Research Square

Preprints are preliminary reports that have not undergone peer review.
They should not be considered conclusive, used to inform clinical practice,
or referenced by the media as validated information.

High-efficiency iodine capture in waste biomass-based activated carbon: Effects of biomass types on iodine adsorption and its mechanism

Runzhuo Liu
Central South University of Forestry and Technology
Liqiang Zhang
21384881@qq.com

Central South University of Forestry and Technology
Xiancheng Ma
Central South University of Forestry and Technology
Liqiang Xia
Central South University of Forestry and Technology
Hongguang Liu
Central South University of Forestry and Technology

Research Article

Keywords: Iodine, Agricultural waste, Porous activated carbons, Adsorption, Pore structure

Posted Date: November 4th, 2026

DOI: https://doi.org/10.21203/rs.3.rs-8341949/v1

License: This work is licensed under a Creative Commons Attribution 4.0 International License.
Read Full License

Additional Declarations: No competing interests reported.

Abstract

The generation of radioactive iodine isotopes during nuclear energy utilization can cause serious harm to the ecological environment and public safety. While porous activated carbon shows promise for iodine capture, balancing its adsorption performance with production costs is a central challenge that hinders its practical adoption in nuclear waste management and emergency response. In this study, porous activated carbons were prepared from agricultural wastes such as rice straw, corn stover, soybean straw, rapeseed straw, and rapeseed cake through hydrothermal carbonization and KOH activation methods. The results showed that the porous activated carbon derived from rapeseed cake (RS) had the highest specific surface area (2025 m^2/g), with iodine adsorption capacities of 5078 mg/g for iodine vapor, 1128 mg/g for iodine in cyclohexane solution, and 2187 mg/g for iodine in aqueous solution. The adsorption of iodine vapor and iodine in aqueous solution was primarily attributed to the micropores and mesopores of the ACs, while iodine adsorption in cyclohexane solution was predominantly governed by micropores of the ACs. Moreover, the adsorption behavior of ACs followed pseudo-second-order kinetics and Langmuir isotherm models, indicating that the adsorption process was primarily physical adsorption. These results provide a theoretical basis for the further design and development of adsorbents for iodine capture from nuclear waste and nuclear accidents, as well as for the high-value utilization of agricultural waste.

1 Introduction

The continuous expansion of the global economy and society continues to drive growth in energy demand. Among low-carbon options, nuclear power offers high energy density and low pollutant emissions, aligning well with China's sustainable development objectives [1–3]. However, nuclear energy inevitably generates radionuclides. Catastrophic events such as the Chernobyl disaster and the Fukushima Daiichi accident led to rapid atmospheric releases of radioactive iodine isotopes (primarily ^{131}I and ^{129}I), posing acute and long-term risks to human health and the environment [4–5]. These incidents underscore the need for robust, high-performance technologies and materials for iodine capture.

Conventional radionuclide management approaches include chemical precipitation, ion exchange, membrane separation, electrochemical treatment, and adsorption. Among these, adsorption is widely considered the most practical and effective route for iodine removal due to its operational simplicity, scalability, and potential for regeneration [6–8]. An optimal adsorbent should provide: (i) high specific surface area with a well-developed and accessible pore network [9–10]; (ii) chemical stability in contact with the adsorbate and process media [11]; and (iii) ease of recovery and mechanical robustness for reuse. Activated carbon (AC) satisfies many of these criteria and is particularly attractive for iodine capture owing to its excellent physicochemical properties, cost-effectiveness, renewability, environmental compatibility, and highly developed porosity [12–15].

Concurrently, rapid agricultural and livestock development generates large volumes of organic waste [16]. In China, technological and logistical constraints result in only about one-third of crop straw being returned to the field via conservation tillage, while the remainder is typically burned directly or indirectly [17–19], creating safety hazards, wasting resources, and causing environmental damage. Converting waste biomass into biochar represents a promising valorization pathway [20]. Biochar is a carbon-rich solid produced through high-temperature pyrolysis/carbonization of industrial/agricultural wastes and plant biomass under oxygen-limited conditions [21–23]. Biochar, recognized for its cost-effectiveness and sustainable nature, serves as a promising adsorbent for radioactive iodine [24–25]. Nevertheless, conventional biochars often exhibit ill-defined, heterogeneous pore networks composed of pyrolytic nanopores and macropores with varying degrees of openness [26]. Such structural disorder constrains accessible surface area and limits maximum adsorption capacity. The variability in biochar pore structures primarily arises from differences in biomass composition and production conditions. Biomass-derived activated carbons display multiscale complexity due to heterogeneous mixtures of cellulose, hemicellulose, and lignin, together with minor components such as extractives and ash, which collectively govern pore development and iodine adsorption behavior [27–28].

Recent studies have begun to elucidate how feedstock composition and processing modulate performance. Can et al. investigated lignin-based biochars with varied cellulose content and found that cellulose addition partially inhibits lignin pyrolysis, increasing biochar yield [29]. However, the optimal cellulose–lignin ratio for producing activated carbons with tailored porosity and iodine affinity remains unresolved, and systematic studies mapping component ratios to structure–property relationships in activated carbon are still lacking. Beyond compositional tuning, functionalization and composite strategies have also been explored. Xiao et al. prepared nitrogen-doped hydrochar from orange peel via urea-assisted hydrothermal synthesis, revealing a linear correlation between increased specific surface area and reduced nitrogen content [30]. Kwak et al. investigated iodine adsorption mechanisms using raw and bismuth-impregnated coffee-ground biochars [31]. Wang et al. synthesized bismuth-based composites from rice husks and demonstrated superior iodine gas capture when carbon served as the carrier [32]. Can et al. optimized production parameters—carbonization temperature, heating rate, activation duration, and activator selection—for coal-based activated carbon to enhance mechanical strength and iodine removal [33]. Xu et al. produced oxygen-rich microporous carbon from cellulose diacetate via hydrothermal carbonization followed by KOH activation, achieving exceptional iodine adsorption capacity [34]. Therefore, the biomass feedstock is a key factor determining the iodine adsorption performance of biomass-derived activated carbon. Moreover, the iodine adsorption mechanisms and performance characteristics of different biomass-derived activated carbons have not yet been comprehensively studied.

In this work, we employ representative agricultural wastes—rice, corn, soybean, and rapeseed straw—and rapeseed cake to produce shaped activated carbons via hydrothermal carbonization and KOH activation. We systematically characterize morphology, pore architecture, and surface chemistry using SEM, TEM, N_2 physisorption, XRD, and XPS, and elucidate structure–reactivity relationships relevant to iodine capture. We quantify iodine adsorption performance and probe the influence of cellulose, hemicellulose,

and lignin contents on capacity and kinetics, thereby identifying an optimal waste biomass-based activated carbon for radioactive iodine removal. This study delivers design principles that couple biomass composition and processing to pore structure and adsorption behavior, providing theoretical and experimental guidance for developing cost-effective adsorbents for gaseous iodine capture and for the sustainable management and valorization of agricultural wastes.

2 Materials and methods

2.1 Reagents and materials

The biomass feedstocks—including rice straw, corn straw, soybean straw, rapeseed straw, and rapeseed cake—adopt for preparing porous biomass-activated carbon. The raw materials of biomass feedstocks were locally sourced from Sichuan Province. All chemical reagents were of analytical grade and used without further purification. Specifically, iodine (I_2) was obtained from Sinopharm Chemical Reagent Co., Ltd.. Potassium hydroxide (KOH) and cyclohexane (C_6H_{12}) were obtained from Aladdin Reagents Ltd.. Deionized water was employed throughout the experiments.

2.2 Preparation of materials

Porous activated carbons were synthesized from five biomass precursors (rice straw, corn straw, soybean straw, rapeseed straw, and rapeseed cake) through sequential hydrothermal carbonization and chemical activation. In the hydrothermal step, each biomass feedstock was mixed with deionized water at a 1:10 mass ratio and processed in a Teflon-lined autoclave maintained at 200°C for 2 hours. After cooling to room temperature, the resulting hydrochar was collected by filtration, washed repeatedly with deionized water, and dried at 105°C overnight. The dried hydrochar was then ground and uniformly mixed with potassium hydroxide at a 1:3 mass ratio before being compacted under 10 MPa pressure. The mixture was transferred to a tubular furnace and first purged with high-purity nitrogen (99.99%) for 30 minutes to establish an inert atmosphere. The thermal activation protocol involved heating to 800°C at a controlled rate of 5°C/min under continuous nitrogen flow, maintaining the target temperature for 1 hour, and then cooling to room temperature at the same rate. The carbonized product subsequently underwent acid washing with 5 wt% hydrochloric acid solution under magnetic stirring for 1 hour to remove residual potassium compounds, and then rinsed thoroughly with deionized water until neutral pH was achieved. Final drying was conducted at 120°C for 8 hours to obtain the activated carbon products. The activated carbons (ACs) were designated as RP (rice straw-derived), CORN (corn straw-derived), SB (soybean straw-derived), RAPE (rapeseed straw-derived), and RS (rapeseed cake-derived) for subsequent characterization and testing.

2.3 Materials characterization

The surface morphology of the prepared samples was analyzed using Scanning Electron Microscopy (SEM, Zeiss Sigma 300) and Transmission Electron Microscopy (TEM, JEOL JEM-F200). Crystalline phase identification was performed by X-ray diffraction (XRD) analysis employing a Rigaku SmartLab SE

diffractometer (Japan) with Cu-Kα radiation (λ = 0.15406 nm) under operating conditions of 40 kV and 40 mA. XRD patterns were collected in the 2θ range of 10–80° with a scanning rate of 5 °/min. Surface chemical composition and functional group analysis were conducted using X-ray photoelectron spectroscopy (XPS, Thermo Scientific Nexsa) with monochromatic Al Kα excitation (1486.6 eV). Textural properties including specific surface area and pore size distribution were determined through nitrogen adsorption-desorption measurements at 77 K using the Brunauer-Emmett-Teller (BET) method, with samples undergoing vacuum degassing at 150°C for 6 hours prior to analysis. Chemical bonding characteristics were investigated by Fourier-transform infrared spectroscopy (FTIR, Thermo Fisher Scientific Nicolet iS20) in the spectral range of 4000 – 400 cm^{-1} with a resolution of 4 cm^{-1}.

2.4 Measurement of lignin content, cellulose and hemicellulose content

Quantitative compositional analysis was performed using the Van Soest method [35]. Samples were initially dried, ground, and sieved to obtain uniform particles. Sequential extraction was then conducted with neutral detergent solution followed by acid detergent solution under reflux conditions. After each extraction step, residues were filtered, thoroughly washed, and dried to yield neutral detergent fiber (NDF) and acid detergent fiber (ADF). The ADF fraction was subsequently treated with 72% sulfuric acid to isolate acid detergent lignin (ADL). Cellulose content was calculated as the mass difference between ADF and ADL, while hemicellulose content was determined from the difference between NDF and ADF. Triplicate measurements were performed for each sample, with results expressed as mean values ± standard deviation. All procedures employed calibrated apparatus with analytical-grade reagents, and method validation was confirmed using certified reference materials.

2.5 Iodine adsorption

The iodine adsorption capacity was evaluated using both vapor-phase and solution-phase methods. For vapor-phase adsorption measurements, approximately 20 mg of adsorbent was placed in a pre-dried and weighed glass vial, while an excess of elemental iodine was added to a separate vial. Both vials were then sealed within an amber glass bottle and maintained at 75°C under atmospheric pressure to simulate nuclear fuel reprocessing conditions. The system was cooled to ambient temperature after specified time intervals (0.5, 1.5, 3, 5, 7, 12, 17, and 24 hours), with iodine uptake quantified gravimetrically according to Eq. 1:

$$\alpha = \frac{1000 \times (m_t - m_1)}{m_0}$$

1

Here,α (mg/g) represents the iodine adsorption capacity; m_1 and m_t are the initial weight of the adsorbent and the change in the weight of the adsorbent after time t, respectively, and m_0 are the sample mass.

To distinguish adsorption mechanisms, iodine-loaded samples were vacuum-desorbed at 125°C for 6 h. The mass loss upon desorption was attributed to physisorbed iodine, while the chemisorbed fraction was calculated by subtracting the physisorption from the total uptake.

For solution-phase studies, cyclohexane was selected as the solvent due to its chemical stability (boiling point = 80.7°C) and demonstrated compatibility with iodine adsorption systems. Standard solutions were prepared by dissolving high-purity iodine (99%) in cyclohexane at concentrations of 3000 mg/L and 5000 mg/L, with subsequent dilutions to 20–100 mg/L for calibration. UV-Vis spectrophotometric analysis at 523 nm yielded the calibration curve described by Eq. 2:

$$y = 0.00409x + 0.00443 (R^2 = 0.999)$$

2

Adsorption isotherms were generated by exposing 5 mg adsorbent samples to 5 mL of iodine/cyclohexane solutions (100–5000 mg/L) in sealed vials. The adsorption capacity was calculated using Eq. 3:

$$Q_e = (C_0 - C_1) \times \frac{\nu}{\omega}$$

3

Here, Q_e(mg/g) represents the adsorption amount of iodine; C_0 and C_1 (mg/L) represents the solution concentration before and after adsorption, respectively, (mL) represents the capacity of iodine/cyclohexane solution, and ω (g) represents the mass of the adsorbent.

Kinetic experiments were conducted at initial iodine concentrations of 100 and 500 mg/L, with aliquots collected at predefined time points over 1–24 h. Temporal adsorption profiles were obtained by quantifying the residual iodine concentration spectrophotometrically at 523 nm against a previously established calibration curve.

Aqueous-phase studies followed similar protocols, utilizing KI-supplemented deionized water as solvent. The corresponding calibration curve followed Eq. 4:

$$y = 0.000409x + 0.00486 (R^2 = 0.957)$$

4

with kinetic measurements conducted at 3000 mg/L initial concentration and sampling intervals of 1–60 minutes.

3 Results and discussion

3.1 Physical and chemical properties of ACs

Figure 1 presents microstructural analysis of RS by SEM and TEM. SEM images (Fig. 1a, b) show that RS has an irregular morphology, with particle sizes ranging from several to tens of micrometers. The surface features a heterogeneous porous texture with cavities spanning a broad size range. High-resolution TEM (Fig. 1c, d) reveals an interconnected, worm-like pore network that pervades the carbon matrix, as well as randomly oriented, slit-shaped micropores within individual particles. These observations confirm a hierarchical pore structure comprising mesoscale cavities and nanoscale micropores, consistent with the effective activation of the biomass-derived carbon.

Figure 2a presents the nitrogen adsorption–desorption isotherms, and Fig. 2b shows the corresponding pore-size distributions for five activated carbons (RP, CORN, SB, RAPE, and RS). All samples exhibit Type I isotherms as classified by IUPAC [36], indicative of predominantly microporous structures. The sharp uptake at low relative pressures ($P/P_0 < 0.1$) confirms the dominance of micropores, whereas the gradual increase in adsorption at intermediate pressures ($0.1 < P/P_0 < 0.5$) indicates the presence of mesoporosity. Pronounced hysteresis loops at higher relative pressures are attributed to the aggressive activation conditions (high KOH/biomass ratio), which promote the development of mesopores (3–5 nm) at the expense of micropores, particularly in the RS sample. Quantitative pore-structure parameters are summarized in Table 1. RS exhibits the highest specific surface area (2025 m^2/g) among the samples, whereas SB has the lowest (1090 m^2/g); the remaining samples display intermediate values (1487–1560 m^2/g). All activated carbons possess substantial total pore volumes (0.492–0.981 cm^3/g), with micropores constituting the majority of the pore structure. Notably, RS combines the largest total pore volume (0.981 cm^3/g) with the lowest micropore fraction (84%), indicating a unique hierarchical porous architecture with well-developed micro- and mesopores.

Table 1
Pore structure parameters and element compositions of ACs

Sample	S_{BET}[a]/m^2/g	V_{total}[b]/mL/g	V_{mic}[e]/mL/g	V_{mic}/V_{total}	O at%	N at%
RP	1487.179	0.665	0.601	0.904	41.12	0.66
CORN	1494.944	0.650	0.600	0.923	28.91	0.61
SB	1090.112	0.492	0.437	0.888	35.49	1.38
RAPE	1559.274	0.669	0.622	0.930	35.28	0.72
RS	2025.110	0.981	0.824	0.840	12.65	1.22

[a] Specific surface area calculated by the BET method. [b] Iota pore volume determined by N_2adsorpton at a relative pressure of 0.99. [c] Micropore volume determined by DFT.

X-ray photoelectron spectroscopy (XPS) characterized the surface chemical composition of the activated carbons (Table 1). Activation at 800°C resulted in low nitrogen contents (0.61–1.38 at%) across all samples, whereas the oxygen content varied substantially among the biomass-derived carbons. RS exhibited the lowest oxygen content (12.65 at%), compared with 28.91–41.12 at% for the other samples. The survey spectra (Fig. 3a) show three characteristic peaks at 284.6 eV (C 1s), 400.5 eV (N 1s), and 533.2 eV (O 1s), with no detectable signals from extraneous elements, indicating compositional uniformity. High-resolution N 1s spectra (Fig. 3c) were deconvoluted into three components—pyridinic N (398.5 ± 0.3 eV), pyrrolic N (400.1 ± 0.2 eV), and graphitic N (401.5 ± 0.4 eV) [37]. Similarly, O 1s spectra (Fig. 3d) were deconvoluted into five components corresponding to carboxyl (531.10 eV), carbonyl (531.9 eV), hydroxyl (533.6 eV), ether (532.65 eV), and adsorbed water (535 eV) [38].

The KOH activation mechanism involves temperature-dependent reactions, with the dominant reactions occurring below 700°C (Eq. 5) [39]. At temperatures below 700°C, KOH decomposition primarily yields inorganic salts such as K_2O and K_2CO_3 (Fig. 3b). Initially, KOH acts primarily as a pore-forming agent. In the 700–800°C range, K_2CO_3 further decomposes into K_2O and metallic potassium (K), with the concomitant release of CO or CO_2 (Eqs. 6–9) [40]. At temperatures between 600 and 900°C, K_2CO_3 reacts with nitrogen-containing functional groups to form NH_3, simultaneously creating a porous structure. This is supported by the observed reduction in nitrogen functional groups within the activated carbon matrix [30, 41]. However, temperatures above 800°C promote pore overactivation and structural collapse, reducing pore volume.

$$6KOH + C \rightarrow 3H_2 + 2K_2CO_3$$

5

$$K_2CO_3 + C \rightarrow K_2O + 2CO$$

6

$$K_2CO_3 \rightarrow K_2O + CO_2$$

7

$$2K + CO_2 \rightarrow K_2O + CO$$

8

$$K_2O + C \rightarrow 2K + CO$$

9

Figure 4a reveals distinct pore characteristics: CORN, SB, and RAPE samples exhibit distributions dominated by micropores (< 10 Å), followed by smaller mesopores (10–20 Å), and larger mesopores (> 20 Å). RP displays a greater proportion of pores below 20 Å. Notably, RS shows a distinctive pattern with

predominant 10–20 Å mesopores and > 20 Å mesopores. This pattern results from the complete reaction between K_2CO_3 and nitrogen-containing functional groups in RS, generating extensive mesopores while accounting for RS's low nitrogen content [40, 42]. Previous studies have reported significant correlations between the lignin, hemicellulose, and cellulose contents of activated carbons (ACs) and their morphological, chemical, and structural characteristics. These compositional differences directly influence adsorption performance, prompting a systematic evaluation of iodine adsorption capacity relative to these three components. Comparative analysis shows that while all AC samples have similar lignin contents and comparable hemicellulose levels (CORN > RS > SB > RAPE), RS exhibits markedly reduced cellulose content at 13.27%, substantially lower than the other samples (Fig. 4b). This profile arises from RS's higher reactivity with KOH, which promotes extensive fibril liberation and cellulose decomposition during activation [43]. Importantly, existing studies confirm that an optimal cellulose-to-lignin ratio facilitates mesopore formation in activated carbons, thereby maximizing adsorption capacity [44].

Fourier-transform infrared (FTIR) spectroscopy was used to characterize the surface functional groups of iodine-loaded RS (RS@I_2). Figure 4c shows that the FTIR spectra of RS and RS@I_2 demonstrate a marked reduction in the intensity of the characteristic peaks of -OH, C = O, aromatic and C-H, concomitant with a shift in the position of the -C = O peak. These modifications implicate iodine capture via electrostatic attraction (oxygen-containing groups), hydrogen bonding (C-H), and π-π conjugation (aromatic frameworks), supplemented by Lewis acid-base interactions where minor N-H and -CN groups function as Lewis bases with iodate ions (Fig. 5). Complementary X-ray diffraction (XRD) was performed to probe potential structural changes upon iodine uptake (Fig. 4d). Both RS and RS@I_2 display similar diffraction patterns with characteristic reflections at 2θ = 25° and 43°, corresponding to the (002) and (100) planes of graphitic carbon [45], indicating graphitic ordering established during carbonization. Notably, RS@I_2 exhibits weaker peak intensities than pristine RS, likely because iodine adsorption disrupts graphitic domains and reduces crystallinity [46].

3.2 Iodine adsorption

To mimic practical nuclear fuel reprocessing conditions, samples were placed in a sealed chamber at 75°C and atmospheric pressure. Iodine vapor adsorption capacity was determined gravimetrically from the mass gain of the adsorbents, and the adsorption kinetics are shown in Fig. 6a. Initially, the capacity increased with time and approached equilibrium by 5 h; however, the RS sample continued to increase significantly between 5 and 24 h. Across the five samples, capacities ranged from 3043 to 5078 mg/g, indicating high iodine uptake. RS exhibited the highest capacity (5078 mg/g), attributable to its rich and well-developed pore structure. RS exhibits a significantly higher adsorption capacity than those of other benchmark materials, including rapeseed pollen-derived activated carbon (3842 mg/g) and orange peel-derived hydrochar (2252 mg/g) [30, 47].

The regeneration of adsorbents is critical for practical deployment. To assess the recyclability of activated carbons (ACs) for iodine vapor capture, iodine-loaded samples underwent vacuum desorption

at 125°C for 6 h, followed by three cycles of adsorption. As shown in Fig. 6b, all ACs maintained high regeneration stability over three cycles. After the first cycle, CORN and RS retained 91.0% and 93.7% of their initial capacities, respectively. CORN preserved 82.9% of its initial capacity after three cycles, whereas RS showed the best overall performance: its third-cycle capacity (3852 mg/g) exceeded the first-cycle capacities of the other samples. These results identify RS as a highly recyclable iodine adsorbent. In contrast, RP, SB, and RAPE exhibited markedly lower capacity in the first cycle. This outcome is likely attributable to their higher macroporosity (Fig. 4a), which can trap iodine molecules deep within the pore network, leading to pore blockage. Similarly, RS, which also possesses high macroporosity (73.9%), exhibits minimal impact on first-cycle adsorption due to its largest total pore volume. CORN has the lowest macroporosity (50.2%). Consequently, after three adsorption cycles, only CORN demonstrates a markedly higher recycling percentage than the other samples.

To further evaluate iodine adsorption by activated carbons (ACs) in the liquid phase, experiments were conducted using iodine dissolved in cyclohexane. The adsorption performance in this system (Fig. 7a) exhibits pronounced concentration dependence: below 2000 mg/L, capacity increases steeply with initial iodine concentration and approaches a plateau above this level. Among the biomass-derived ACs, RAPE shows the highest saturation capacity (1148 mg/g), closely followed by RS (1128 mg/g). Kinetic tests at 100 and 500 mg/L provide additional insight. In the 500 mg/L solution, the color changed from purple to lilac, indicating effective iodine removal (Fig. 7b). The kinetic profiles show rapid uptake, reaching equilibrium within 7 h at 100 mg/L and within 5 h at 500 mg/L (Fig. 7c and 7d). RS achieved removal efficiencies of 97% and 75% at 100 and 500 mg/L, respectively, underscoring its potential for extracting iodine from organic solutions.

Figure 8a shows the concentration-dependent adsorption behavior of the activated carbons (ACs). Iodine uptake increased with the initial solution concentration up to 3000 mg/L, after which the rate of increase diminished. RS exhibited superior performance among the biomass-derived ACs, reaching a maximum capacity of 2187 mg/g at 5000 mg/L. Kinetic analysis at 3000 mg/L (Fig. 8b) indicates that most ACs reached equilibrium within approximately 10 min, whereas RS and RP required about 30 min. Despite the slower kinetics, RS maintained a high-capacity of 2066 mg/g, substantially exceeding the other samples. Visual observations corroborate effective iodine removal, with the solution color changing from dark red to light red; in the case of RS, the color further shifted to light yellow (Fig. 8c).

3.3 Adsorption kinetics

The adsorption mechanisms of five biomass-derived activated carbons were evaluated by kinetic modeling. Both the pseudo-first-order (PFO) and pseudo-second-order (PSO) models fit the experimental data well (Fig. 9; Table 2; Table 3;Table 4), with the PSO model providing the best correlation (R^2 = 0.99). These results indicate that PSO more appropriately describes iodine adsorption on the ACs. The parameter fitting results demonstrate that the adsorption process is governed by multiple mechanisms [48, 49]. Iodine adsorption kinetics by activated carbons in vapor, aqueous, and cyclohexane media are governed by three rate-controlling steps: external mass transfer (film diffusion), chemisorption on

surface sites, and intraparticle diffusion. At the outset, rapid uptake occurs via surface adsorption driven by abundant active sites and steep concentration gradients. As adsorption proceeds, the process becomes increasingly controlled by intraparticle diffusion, owing to the depletion of accessible sites, lower iodine concentration, and reduced mass-transfer driving force. Equilibrium is reached when adsorption and desorption rates balance, yielding a constant residual iodine concentration and a saturated adsorption capacity.

Table 2
Parameters of kinetic models for iodine adsorption on ACs iodine vapor adsorption

Sample	Pseudo-first-order model			Pseudo-second-order model		
	$k_1(h^{-1})$	$q_e(mg/g)$	R^2	$K_2\ (h^{-1})$	$q_e(mg/g)$	R^2
RP	1.035	3602	0.917	2.514E-4	3841	0.999
CORN	1.100	3366	0.932	2.826E-4	3458	0.998
SB	0.602	3002	0.961	3.035E-4	3107	0.989
RAPE	1.195	3349	0.924	2.932E-4	3361	0.998
RS	0.338	4816	0.984	1.740E-4	5097	0.990

Table 3
Parameters of kinetic models for iodine adsorption on ACs from cyclohexane solution.

Sample	Pseudo-first-order model			Pseudo-second-order model		
	$k_1(h^{-1})$	$q_e(mg/g)$	R^2	$K_2\ (h^{-1})$	$q_e(mg/g)$	R^2
RP	1.299	81	0.978	0.0117	84	0.999
CORN	0.942	88	0.968	0.0108	91	0.999
SB	1.562	86	0.966	0.0113	87	0.999
RAPE	0.865	90	0.983	0.0105	92	0.999
RS	0.996	91	0.959	0.0099	97	0.999

Table 4
Parameters of kinetic models for iodine adsorption on ACs from I_2/KI solutions

Sample	Pseudo-first-order model			Pseudo-second-order model		
	$k_1(h^{-1})$	q_e(mg/g)	R^2	K_2 (h^{-1})	q_e(mg/g)	R^2
RP	0.151	1095	0.930	7.965E-4	1158	0.997
CORN	0.781	1217	0.951	7.846E-4	1258	0.999
SB	0.667	1294	0.954	7.313E-4	1345	0.999
RAPE	0.486	1043	0.933	8.845E-4	1100	0.999
RS	0.432	1972	0.922	4.696E-4	2072	0.999

Isothermal adsorption of iodine from cyclohexane solutions was used to further evaluate the adsorption behavior of the activated carbons (ACs). Comparison of the Langmuir and Freundlich isotherms (Fig. 10; Table 5; Table 6) showed that the Langmuir model provided the better fit to the experimental data, as evidenced by its higher R^2 and the closer agreement between calculated and measured capacities. This result indicates that the Langmuir model more accurately describes iodine adsorption in this system. In the Langmuir framework, iodine molecules form a monolayer on a homogeneous surface with uniform adsorption sites on the activated carbon [50].

Table 5
Langmuir and Freundlich isotherm parameters for iodine adsorption (cyclohexane solution)

Sample	Langmuir			Freundlich		
	Q_m (mg/g)	b (mg^{-1})	R^2	K	n	R^2
RP	1248	7.552E-4	0.980	18.77	0.472	0.910
CORN	1470	6.755E-4	0.984	18.27	0.491	0.927
SB	1298	7.588E-4	0.982	19.79	0.470	0.917
RAPE	1582	6.693E-4	0.984	19.27	0.493	0.924
RS	1545	6.794E-4	0.985	19.38	0.490	0.926

Table 6
Langmuir and Freundlich isotherm parameters for iodine adsorption (I_2/KI solution)

Sample	Langmuir			Freundlich		
	Q_m (mg/g)	b (mg^{-1})	R^2	K	n	R^2
RP	3585	1.718E-4	0.994	3.792	0.716	0.997
CORN	3232	2.411E-4	0.982	5.964	0.672	0.982
SB	3002	2.598E-4	0.994	5.683	0.673	0.971
RAPE	5976	8.270E-5	0.987	1.873	0.803	0.994
RS	3999	2.666E-4	0.979	7.284	0.679	0.943

4 Conclusion

Comprehensive characterization and adsorption studies identify RS-derived activated carbon as the best-performing material among the evaluated biomass precursors, with superior textural properties (specific surface area 2025 m^2/g; total pore volume 0.981 cm^3/g). This structural advantage translates into high iodine adsorption capacities across phases: 5078 mg/g (vapor), 1126 mg/g (cyclohexane), and 2187 mg/g (aqueous). Characterization of activation chemistry indicates that nitrogen-containing functional groups primarily enhance pore development by reacting with K_2CO_3 during activation, rather than acting as primary adsorption sites. Combined experimental and theoretical evidence shows that vapor-phase adsorption is dominated by micropore and narrow mesopore volumes (< 3 nm), with heteroatom doping exerting minimal influence. In aqueous systems, narrow mesopores govern capacity, whereas oxygen-containing groups increase surface polarity and promote competitive water adsorption. In cyclohexane, adsorption correlates strongly with micropore accessibility. RS's distinctively low cellulose content facilitates extensive reactions with KOH that preferentially generate mesopores. Although hemicellulose and lignin contents are comparable to those of other precursors, RS achieves maximal adsorption through an optimal cellulose-to-lignin ratio that favors mesopore formation. Kinetic analysis indicates that pseudo-second-order behavior (R^2 > 0.98) predominates over pseudo-first-order, consistent with combined physisorption and chemisorption. Both liquid-phase adsorption systems follow the Langmuir isotherm (R^2 > 0.95), consistent with monolayer adsorption.

Declarations

CRediT authorship contribution statement

Runzhuo Liu: Writing-original draft, Investigation, **Liqiang Zhang**:Methodology, Investigation, Data curation, **Xiancheng Ma**: Writing-review & editing, Methodology, Investigation. **Liqiang Xia**: Methodology. **Hongguang Liu**: Writing-review&editing, Investigation.

Declaration of competing interest

The authors declare that they have no known competing financialinterests or personal relationships that could have appeared to influencethe work reported in this paper.

Acknowledgments

This work was supported by the Regional Joint Funds of Natural Science Foundation of Hunan Province (No. 2024JJ7640).

Data Availability

Data will be made available on request.

References

1. Morgan FWJB (2022) A.J. S., et al., Current status of university-based energy institutes in the United States and a pathway to forming a national organization, vol 25. iScience, p 104151
2. Mustafa N (2022) Corrigendum to The impact of nuclear energy use, energy prices and energy imports on CO2 emissions: Evidence from energy importer emerging economies which use nuclear energy. J Clean Prod, 379
3. Nanami N, Shoki K, Eiji Y (2022) Life cycle resource use of nuclear power generation considering total material requirement. J Clean Prod, 363
4. Miensah ED, Khan MM, Chen JY et al (2019) Zeolitic imidazolate frameworks and their derived materials for sequestration of radionuclides in the environment: A review. Crit Rev Environ Sci Technol 50:1874–1934
5. Chebbi M, Azambre B, Volkringer C et al (2018) Dynamic sorption properties of metal-organic frameworks for the capture of methyl iodide. Microporous Mesoporous Mater 259:244–254
6. Wang C, Hu H, Chen M et al (2022) Active ion-exchangeable Bi2O(OH)2SO4 synthesized by ball milling for effective iodine enrichment: Insight into the pathway. J Nucl Mater, 572
7. Sarah JTRK, Joshua T et al (2023) Radioiodine abatement – Development of radioiodine targeting strategies in the light of zero emission. Prog Nucl Energy, 165
8. Huve J, Ryzhikov A, Nouali H et al (2018) Porous sorbents for the capture of radioactive iodine compounds: A review. RSC Adv 8:29248–29273
9. Zuo S, Zhang W, Wang Y et al (2020) Low-cost preparation of high-surface-area nitrogen-containing activated carbons from biomass-based chars by ammonia activation. Ind Eng Chem Res 59:7527–7537

10. Lili S, Xilong L, Jian M et al (2022) N-doping high specific surface area microporous carbon materials derived from gram-positive bacteria and its outstanding performance for supercapacitors. Ceram Int 48:7265–7272
11. Tingting X, Yuanyuan W, Qian Z et al (2024) Ti3C2Tx MXene-derived hydroxyl-rich titanate based hybrid membrane with cellulose as structural regulator for highly-efficient disposition of heavy metal ions. Desalination, 572
12. Baogen L, Xiancheng M, Da W et al (2022) Development of ultramicropore–mesopore interconnected pore architectures for boosting carbon dioxide capture at low partial pressure. Carbon 192:41–49
13. Junying L, Baogen L, Rui S et al (2021) The effects of nitrogen functional groups and narrow micropore sizes on CO2 adsorption onto N-doped biomass-based porous carbon under different pressure. Microporous Mesoporous Mater, 327
14. Wang J, Kong H, Zhang J et al (2020) Carbon-based electrocatalysts for sustainable energy applications. Prog Mater Sci, 116
15. Adaobi IOJIOKCI et al (2021) Verification of pore size effect on aqueous-phase adsorption kinetics: A case study of methylene blue. Colloids Surf A, 626
16. Kunwar P, Monika KSKY et al (2017) Food waste to energy: An overview of sustainable approaches for food waste management and nutrient recycling. Biomed Res Int 2017:2370927
17. Manisha K, Ram GC, Savita C et al (2022) Transformation of waste rice straw to carbon quantum dots and their potential chemical sensing application: Green and sustainable approach to overcome stubble burning issues. Biomass Convers Biorefinery 14:7507–7518
18. Sun J, Peng H, Chen J et al (2016) An estimation of CO2 emission via agricultural crop residue open field burning in China from 1996 to 2013. J Clean Prod 112:2625–2631
19. Kai Z, Bintong Y, Xiaoting Y (2023) The agricultural–ecological benefit of digital inclusive finance development: Evidence from straw burning in China, Sustainability, 15 3242
20. Ran Z, Haoxiang W, Jie J et al (2022) Viscoelastic properties, rutting resistance, and fatigue resistance of waste wood-based biochar-modified asphalt. Coatings 12:89
21. Zhu Z, Xu Z (2020) The rational design of biomass-derived carbon materials towards next-generation energy storage: A review. Renew Sustain Energy Rev, 134
22. Ping YG, Bo ZZ, Jing KH et al (2017) Energy storage applications of biomass-derived carbon materials: Batteries and supercapacitors. New J Chem 41:11456–11470
23. Islam AM, Auta M, Kabir G et al (2016) A thermogravimetric analysis of the combustion kinetics of karanja (Pongamia pinnata) fruit hulls char. Bioresour Technol 200:335–341
24. Li C, Zhang L, Gao Y et al (2018) Facile synthesis of nano ZnO/ZnS modified biochar by directly pyrolyzing of zinc contaminated corn stover for Pb(II), Cu(II) and Cr(VI) removals. Waste Manag 79:625–637

25. Jibo D, Yao T, Zhijiang L et al (2023) Neglected but efficient electron utilization driven by biochar-coactivated phenols and peroxydisulfate: Polyphenol accumulation rather than mineralization. Environmental Science & Technology, p 57
26. Gray M, Johnson GM, Dragila IM et al (2014) Water uptake in biochars: The roles of porosity and hydrophobicity. Biomass Bioenergy 61:196–205
27. Wang S, Dai G, Yang H et al (2017) Lignocellulosic biomass pyrolysis mechanism: A state-of-the-art review. Prog Energy Combust Sci 62:33–86
28. Yongtao Y, Chunfeng D, Zhansheng W et al (2018) Relationship of cellulose and lignin contents in biomass to the structure and RB-19 adsorption behavior of activated carbon. New J Chem 42:16493–16502
29. Can Z, Lichao G, Ruikun W et al (2023) Effects of cellulose addition on the physicochemical properties, pore structure and iodine adsorption of lignin-based biochar. Fuel, 352
30. Xiao K, Liu H, Li Y et al (2020) Excellent performance of porous carbon from urea-assisted hydrochar of orange peel for toluene and iodine adsorption. Chem Eng J 382:122997
31. Jinwoo J, SangHo L, Jaegwan S et al (2022) Synthesis and applications of bismuth-impregnated biochar originated from spent coffee grounds for efficient adsorption of radioactive iodine: A mechanism study. Environ Pollut 313:120138
32. Wang E, Li C, Hou X et al (2023) Capture of iodine gas by Bi-based composites derived from rice husk: Influence of the type of support on the iodine adsorption and retention. Chem Eng J, 465
33. Can Z, Lichao G, Mingjin Z et al (2023) Study on the mechanical strength and iodine adsorption behavior of coal-based activated carbon based on orthogonal experiments. Energy, 282
34. Zhanglian X, Qian Z, Peng L et al (2022) Oxygen-rich microporous carbons with exceptionally high adsorption of iodine. Mater Chem Phys, 285
35. Van Soest PJ (1963) Use of detergents in the analysis of fibrous feeds. II. A rapid method for the determination of fiber and lignin. J Association Official Agricultural Chem 46:829–835
36. Kärger J, Valiullin R, Brandani S et al (2025) Diffusion in nanoporous materials with special consideration of the measurement of determining parameters (IUPAC Technical Report), Pure and Applied Chemistry, 97 1–89
37. Li L, Ma X, Chen R et al (2018) Nitrogen-containing functional groups-facilitated acetone adsorption by ZIF-8-derived porous carbon. Materials 11:159
38. Qiang Y, Guo L, Li H et al (2021) Fabrication of environmentally friendly Losartan potassium film for corrosion inhibition of mild steel in HCl medium. Chem Eng J 406:126863
39. Lillo-Ródenas M, Cazorla-Amorós D, Linares-Solano A (2003) Understanding chemical reactions between carbons and NaOH and KOH. Carbon 41:267–275
40. Chen W et al (2020) Insight into KOH activation mechanism during biomass pyrolysis: Chemical reactions between O-containing groups and KOH. Appl Energy 278:115730

41. Sevilla M, Ferrero AG, Diez N et al (2018) One-step synthesis of ultra-high surface area nanoporous carbons and their application for electrochemical energy storage. Carbon 131:193–200
42. Dong X, Chu Y, Tong Z et al (2024) Mechanisms of adsorption and functionalization of biochar for pesticides: A review. Ecotoxicol Environ Saf 272:116019
43. Lazić DB, Pejić MB, Kramar DA et al (2018) Influence of hemicelluloses and lignin content on structure and sorption properties of flax fibers (Linum usitatissimum L.), Cellulose, 25 697–709
44. Yongtao Y, Chunfeng D, Zhansheng W et al (2018) Relationship of cellulose and lignin contents in biomass to the structure and RB-19 adsorption behavior of activated carbon. New J Chem 42:16493–16502
45. Xiancheng M, Changqing S, Baogen L et al (2021) Heteroatom-doped porous carbons exhibit superior CO2 capture and CO2/N2 selectivity: Understanding the contribution of functional groups and pore structure. Sep Purif Technol 259:118065
46. Kim J, Kim JK, Bae J et al (2024) Experimental and numerical investigation of cryogenic no-vent fill (NVF) process using adsorption on activated carbon. Cryogenics 139:103806
47. Juncheng, Ma et al (2024) Biomass derived porous carbon for efficient iodine adsorption from vapor and solution. Sep Purif Technol 347:127613
48. Yao W, Wu Y, Pang H et al (2018) In-situ reduction synthesis of manganese dioxide@polypyrrole core/shell nanomaterial for highly efficient enrichment of U(VI) and Eu(III). Sci China Chem 61:812–823
49. Chenlu Z, Xing L, Zhongshan C et al (2018) Synthesis of ordered mesoporous carbonaceous materials and their highly efficient capture of uranium from solutions. Sci China Chem 61:281–293
50. Langmuir I (1916) The dissociation of hydrogen into atoms. III. The mechanism of the reaction. J Am Chem Soc 38:1145–1156

Figures

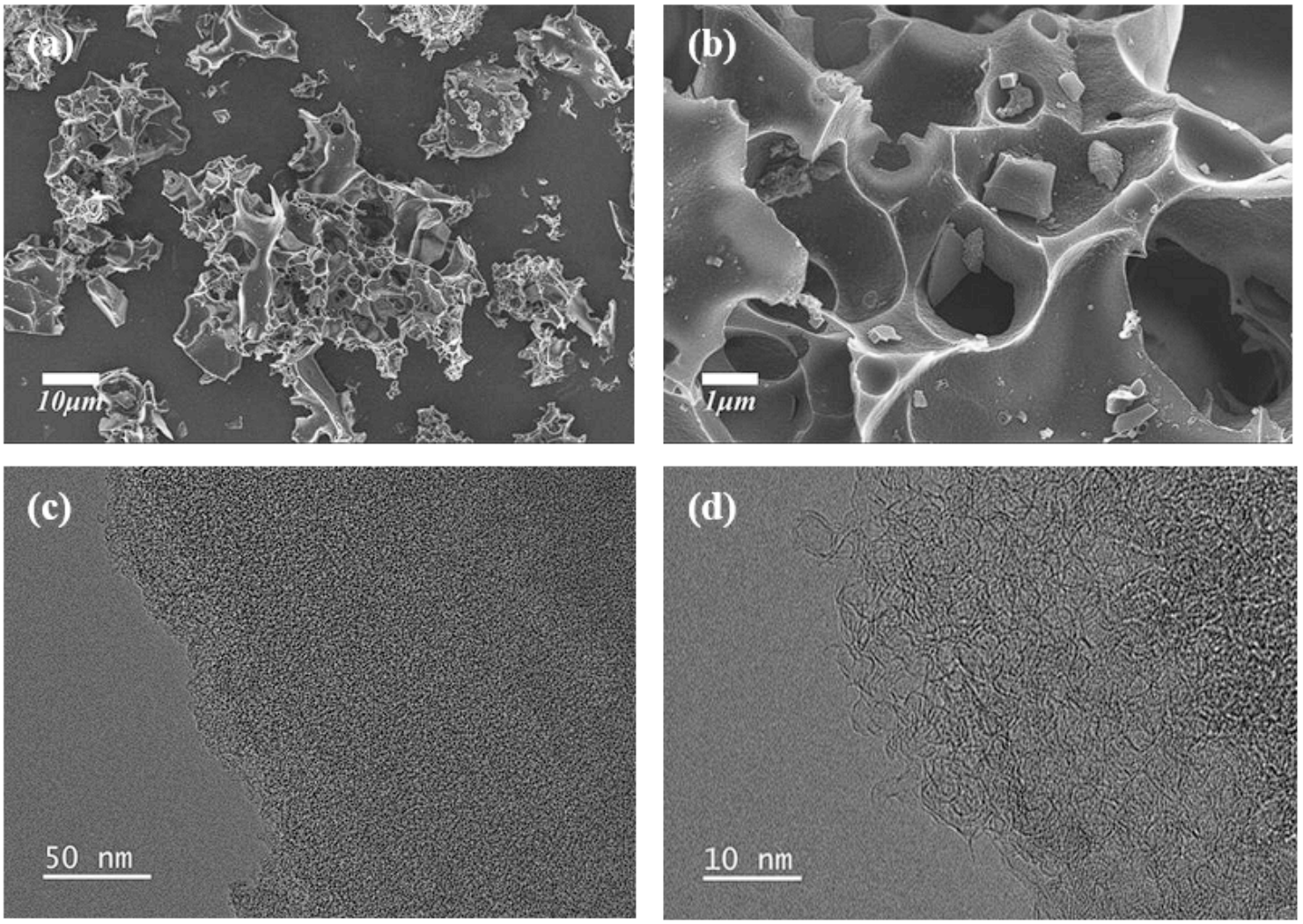


Figure 1

(a-b) SEM images; (c-d) TEM images

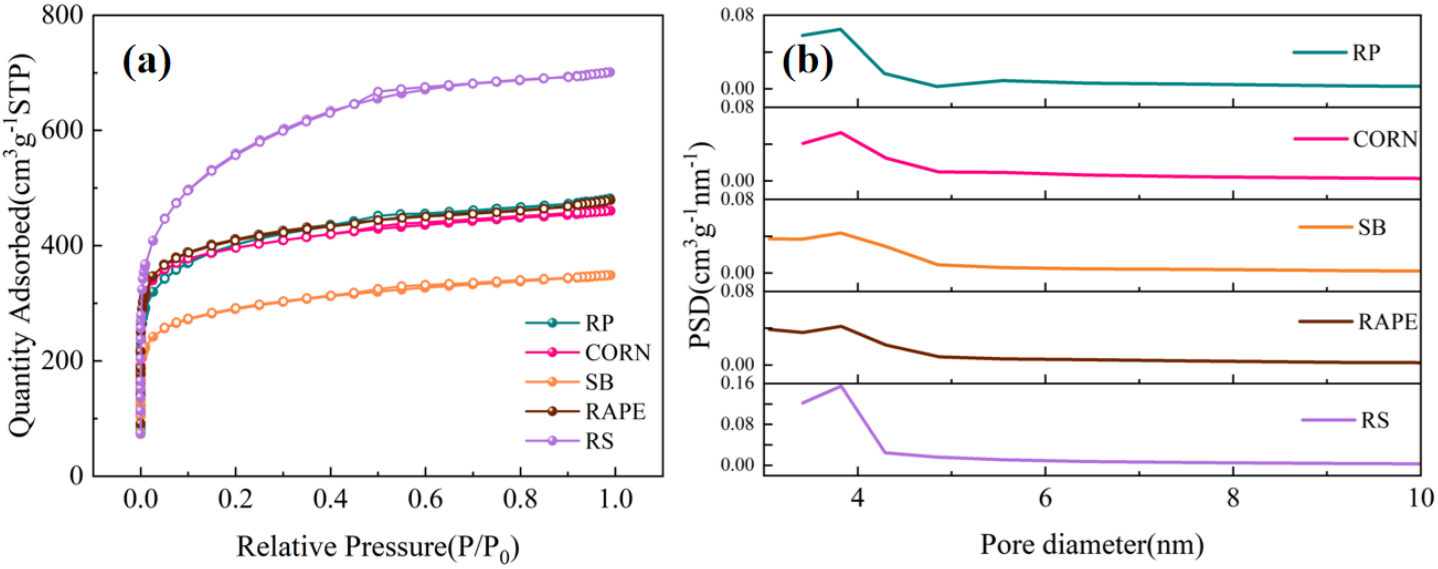


Figure 2

(a) Nitrogen adsorption and desorption isotherms of ACs ;(b) Pore size distributions curves

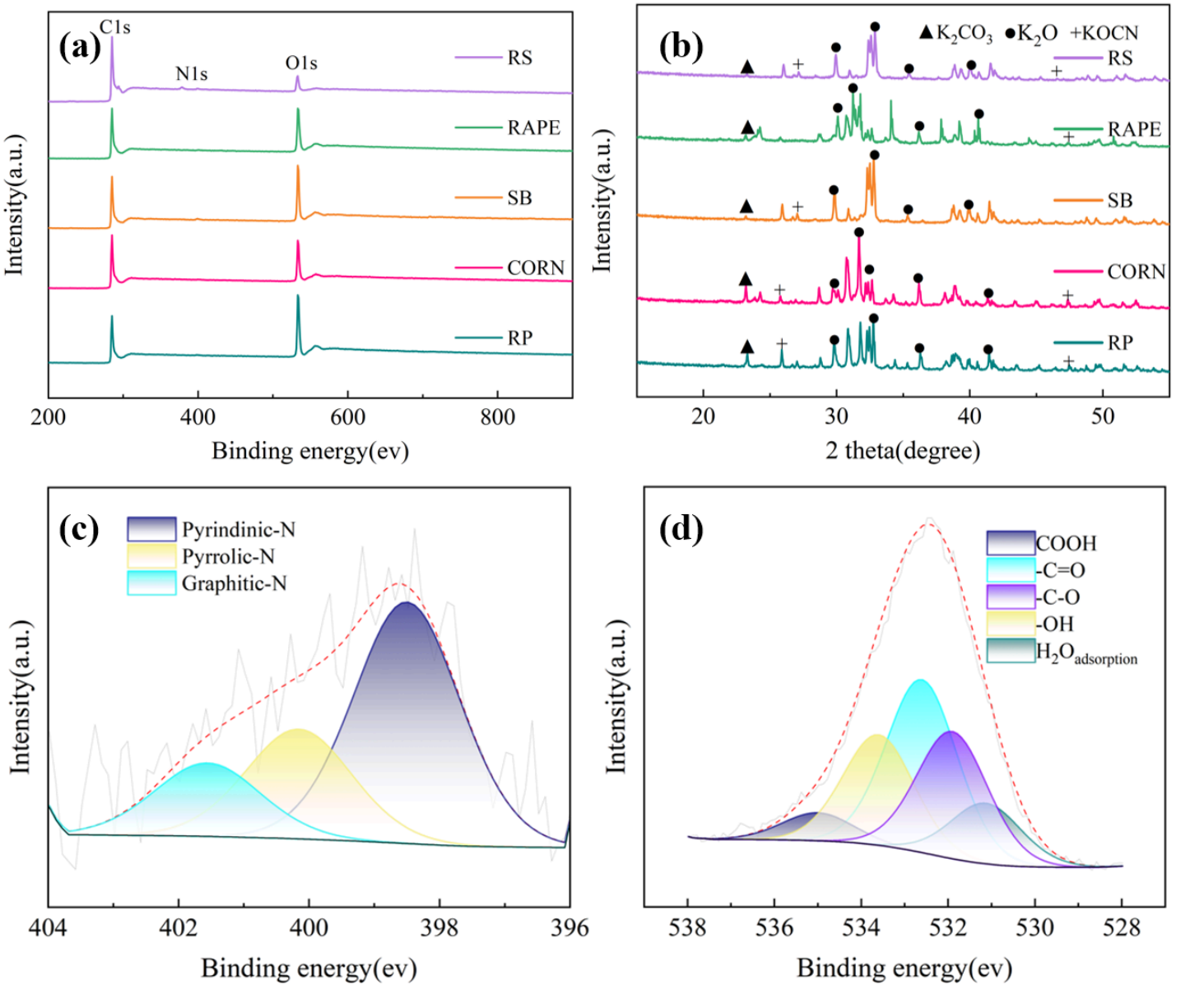


Figure 3

(a) XPS spectra of ACs;(b) XRD patterns of the ACs with and without HCl treatment ; N 1s spectra of the NBC samples (c) RS and O 1s spectra of the NBC samples (d) RS.

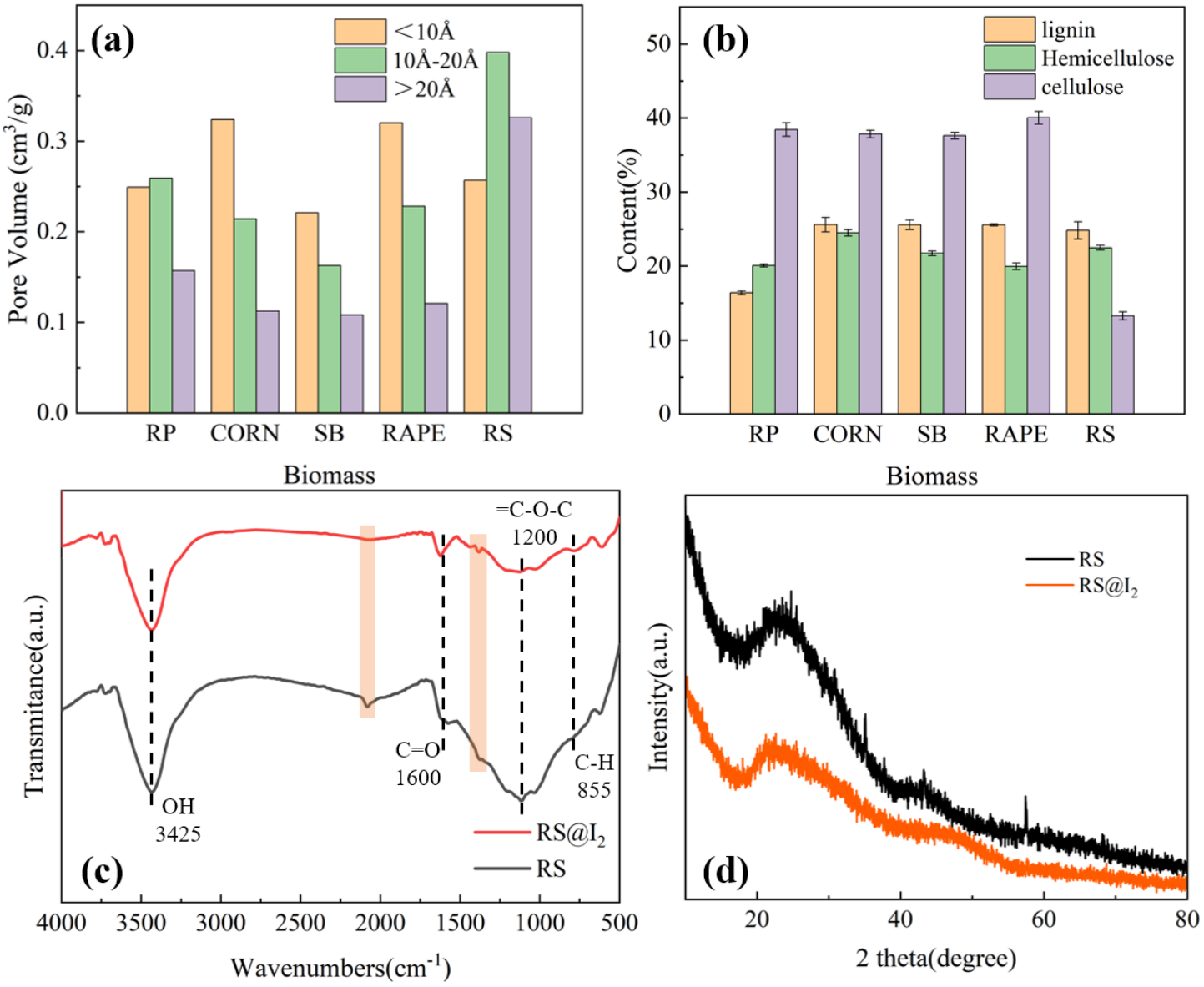


Figure 4

(a) The relationship between pore size distribution and different biomass ACs;(b) The content of lignin, hemicellulose and cellulose in each ACs; (c) The FTIR spectra of RS and RS@I_2;(d) XRD pattern of RS and RS@I_2.

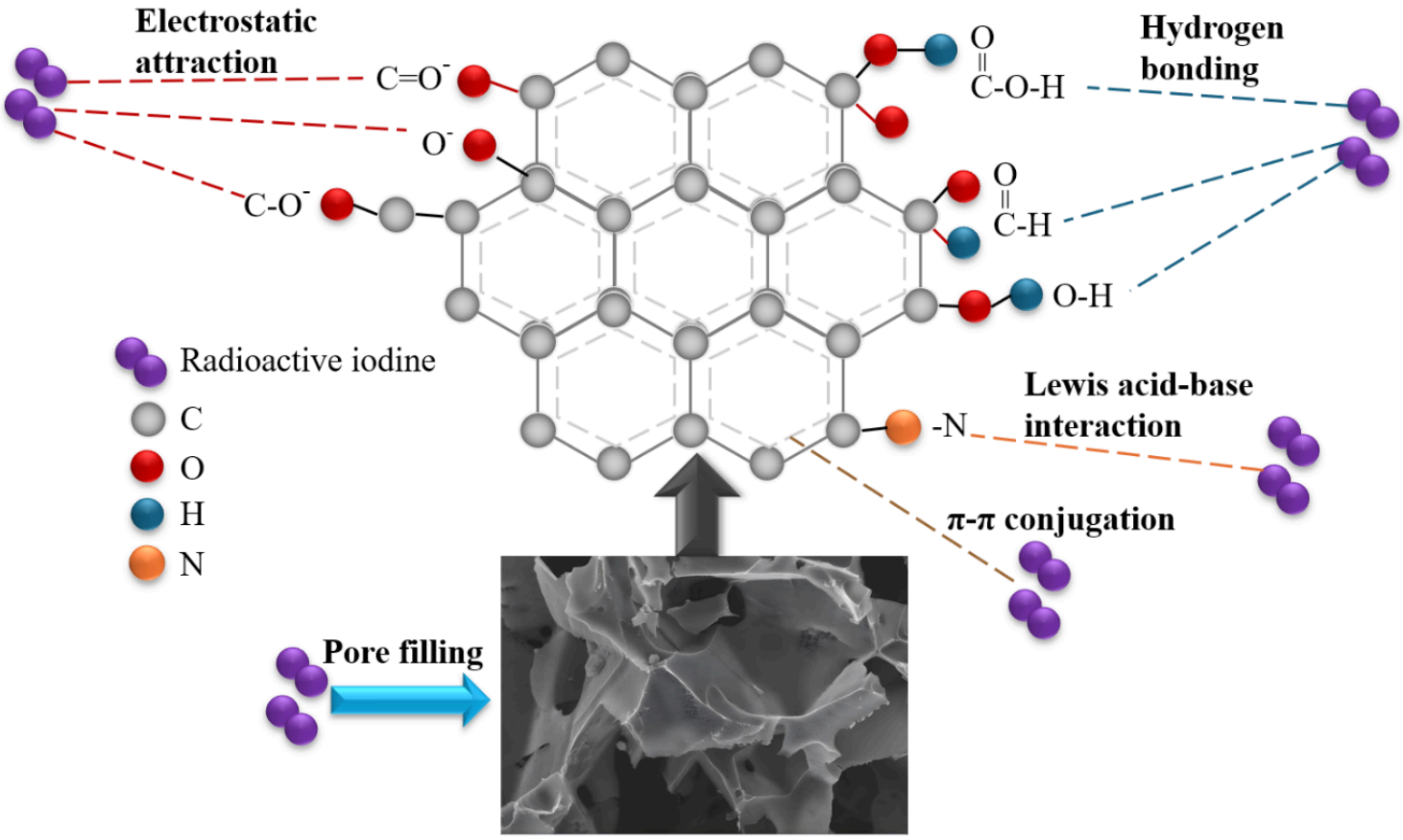


Figure 5

The capture mechanism of ACs

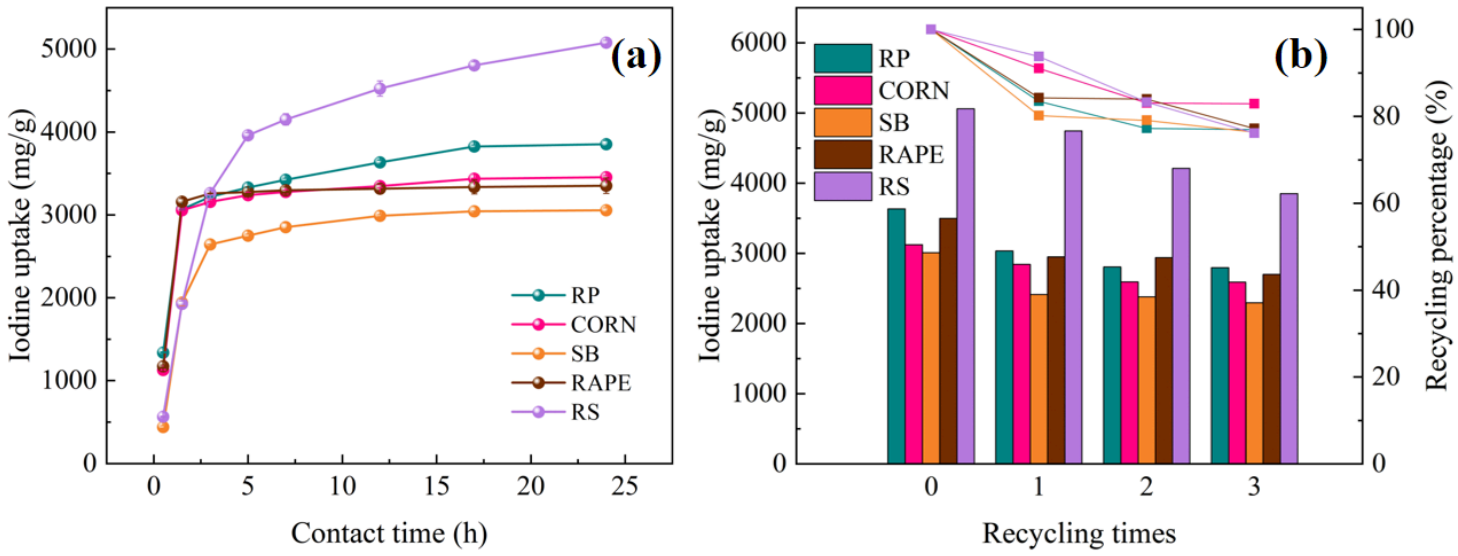


Figure 6

Iodine vapor adsorption of ACs: (a) adsorption curve at 75 °C; (b) cyclic performance after 3 runs.

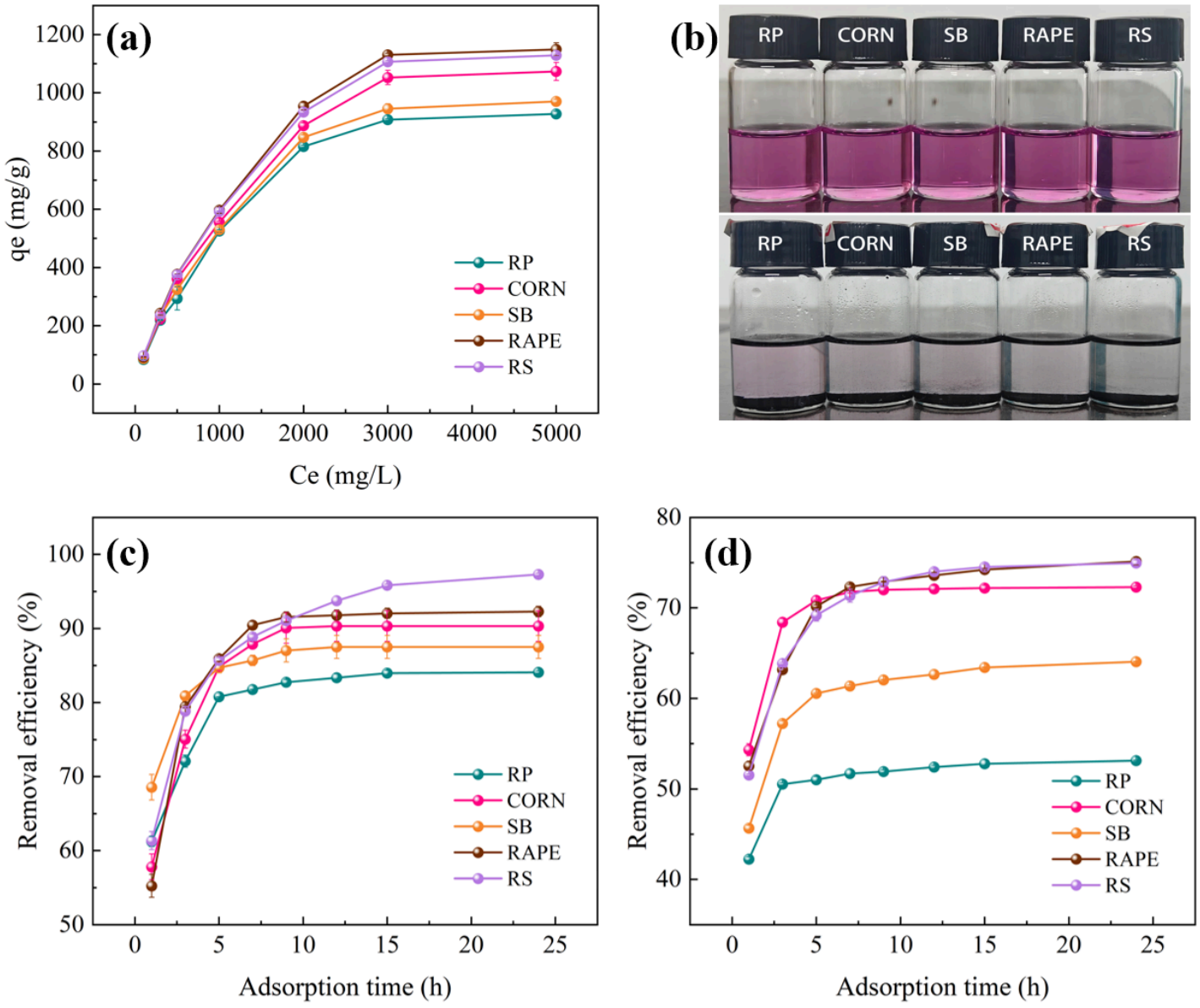


Figure 7

(a) Iodine adsorption isotherm of ACs (5 mg in 5 mL solution, 24 h); (b) Visual comparison of the iodine/cyclohexane solution (100 mg/L) before and after adsorption;(c, d) Iodine removal kinetics by ACs at initial concentrations of 100 and 500 mg/L.

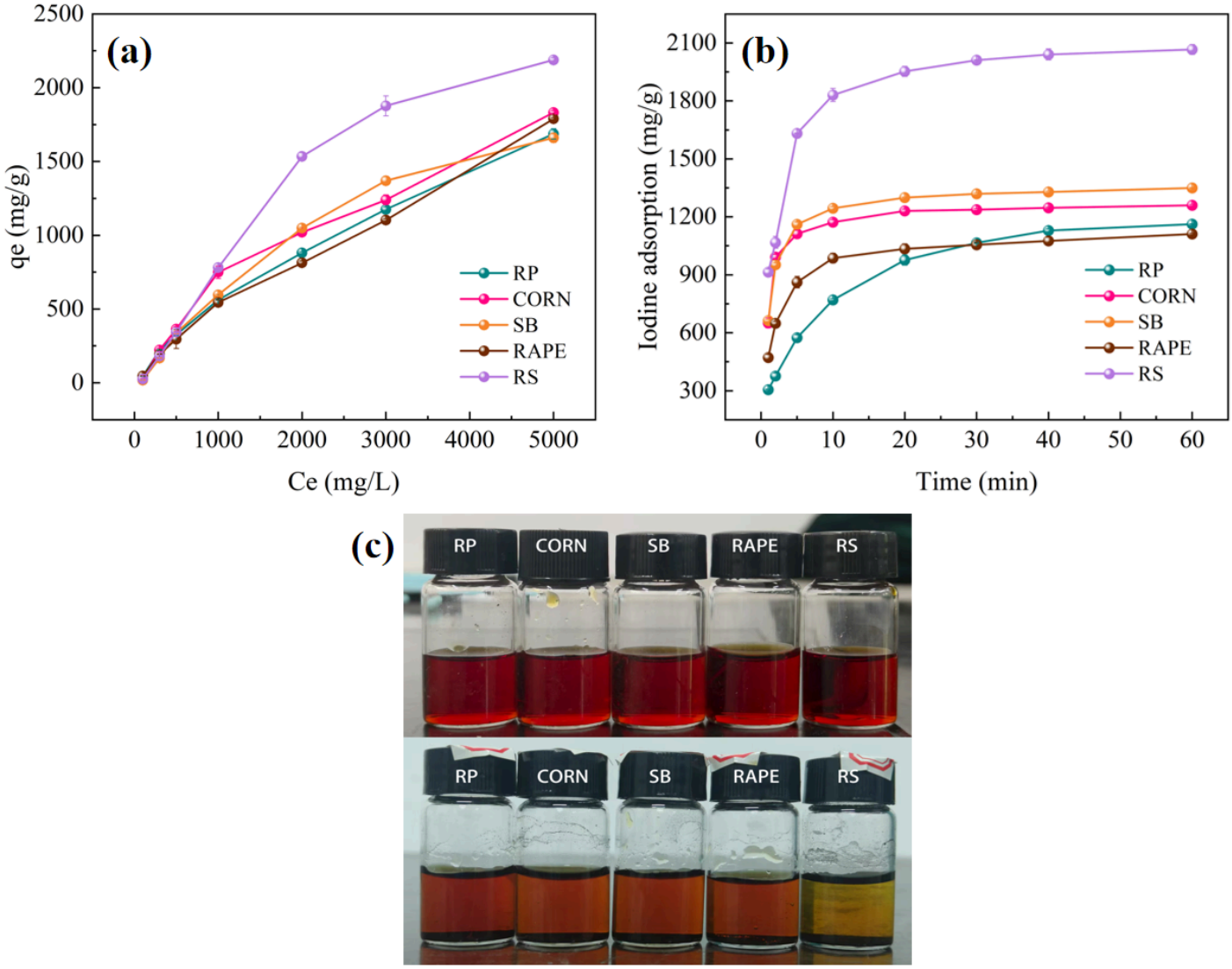


Figure 8

(a) Iodine adsorption isotherm, (b) adsorption kinetics, and (c) visual decolorization of I_2/KI solutions by ACs. (Experimental condition for isotherm: 5 mg ACs in 5 mL solution with 1 h contact time).

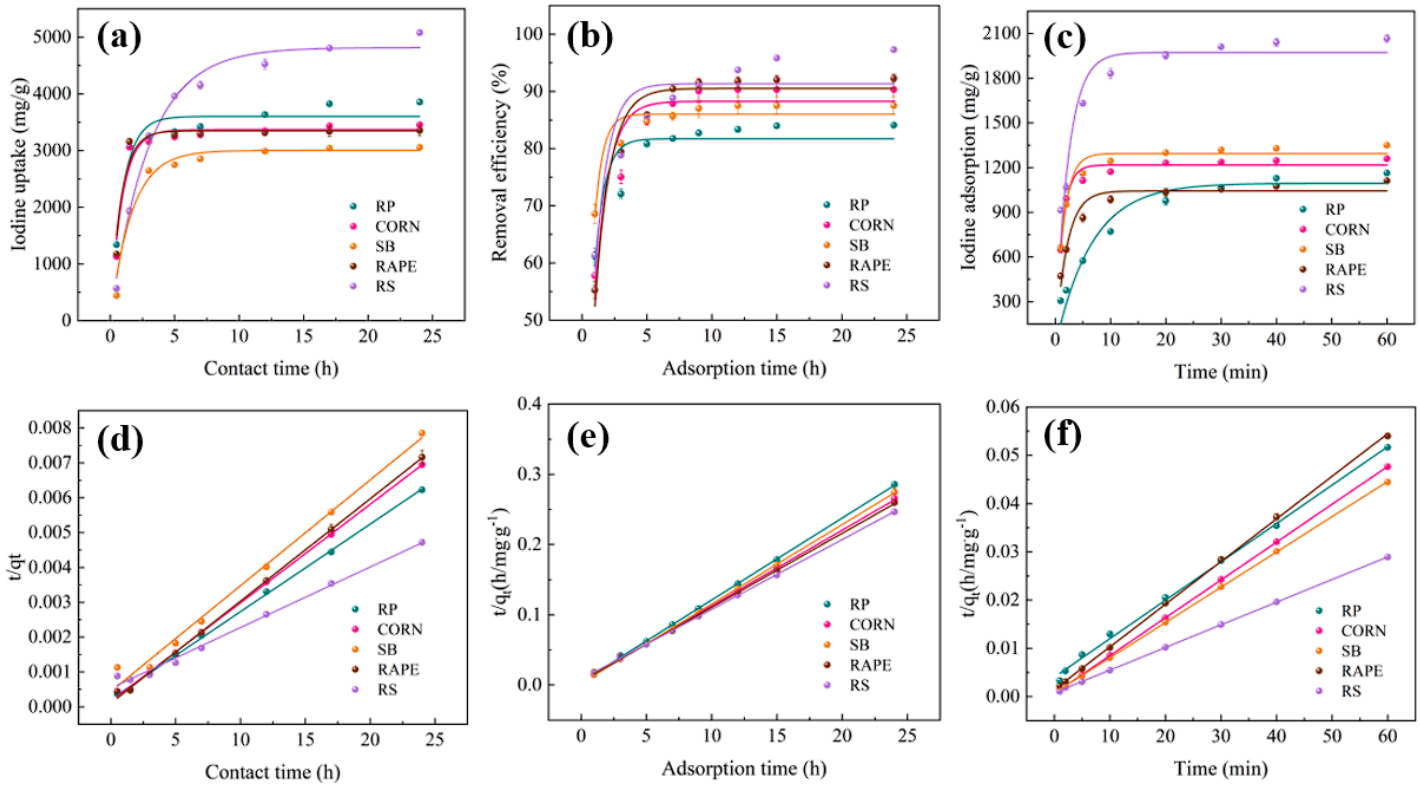


Figure 9

Pseudo-first-order model of adsorbents for iodine absorption in (a) iodine vapor;(b) iodine/cyclohexane; (c) I_2/KI solutions; pseudo-second-order model of adsorbents for iodine absorption in (d) iodine vapor; (e) iodine/cyclohexane;(f) I_2/KI solutions.

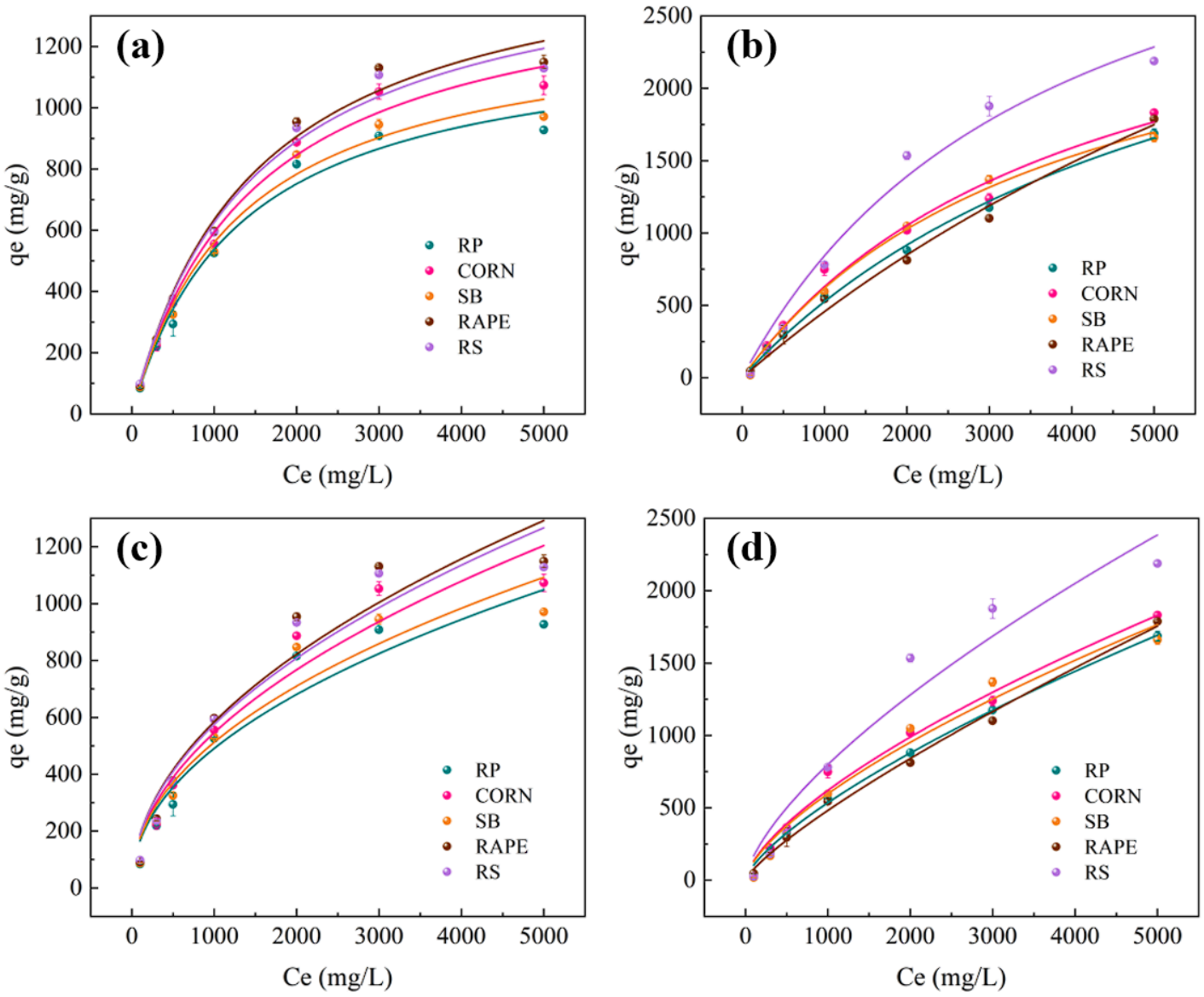


Figure 10

Langmuir and Freundlich isotherm fits for iodine adsorption on ACs in (a, c) cyclohexane and (b, d) I_2/KI solutions.

Supplementary Files

This is a list of supplementary files associated with this preprint. Click to download.

- attachment.docx